RSC Advances

PAPER

View Article Online
View Journal | View Issue

Cite this: *RSC Adv.*, 2015, **5**, 46405

Gold loaded titanium dioxide–carbon nanotube composites as active photocatalysts for cyclohexane oxidation at ambient conditions†

Mohamed Mokhtar Mohamed*

Photocatalytic oxidation of neat cyclohexane (CHA) with H_2O_2 as an oxidant was carried out using gold modified versions of several types of materials, including titania nanotubes (Au/TNT), reduced graphene oxide (Au/RGO) as well as titania nanotubes–multiwalled carbon nanotubes composite (Au/TNT–MWCNT) under UV irradiation (125 W, $\lambda > 296$ nm). The synthesized nanoparticles were characterized using physical adsorption of nitrogen, X-ray diffraction, transmission electron microscopy and ultraviolet-visible diffuse reflectance spectroscopy, and the reaction products were analyzed by GC-MS. Both Au/RGO and Au/TNT–MWCNT catalysts promoted partial CHA oxidation with higher conversion (6–9.0%) and selectivity (60–75%) for cyclohexanone, exceeding Au/TNT, TNT–MWCNT and TNT catalysts (conv. 2.1–4%, sel. 32–55%). Au/TNT–MWCNT synthesized using hydrothermal deposition methods exhibited the highest catalytic activity. This was chiefly attributable to the high surface hydrophobicity of MWCNT that accelerated CHA adsorption, bonding of cyclohexanol and cyclohexanone to TNT as well as decomposition of H_2O_2 on gold nanoparticles. Increasing the surface area as well as decreasing the average particle size of Au^0 to 15 nm of hexagonal shape contributed to the superior catalytic activity of Au/TNT–MWCNT, in achieving an average rate of 0.0035 $mmol^{-1}$ g^{-1} min^{-1} and conversion was 9.0% after 12 h of reaction. The latter catalyst exceeded industrially synthesized Co based catalysts (3.6%) operated at high temperatures. For confirming the autoxidation process, a radical scavenger offered a proof that the oxidation follows a radical-chain mechanism. The differences in surface morphology, light absorption and surface properties of Au/TNT when incorporated with MWCNT were well investigated. The photocatalytic oxidation mechanism elucidated using active scavengers suggested that $OH^{\bullet}$ and $O_2^{\bullet-}$ play key roles in the oxidation of CHA.

Received 24th March 2015
Accepted 7th May 2015

DOI: 10.1039/c5ra05253j

www.rsc.org/advances

1. Introduction

Titanium oxide nanotubes (TiO_2 nanotube, TNT) are one of the promising nanostructured oxides with a tubular shape with almost no absorption in the visible light region.[1] Instead, its UV light-sensitive inducing chemical reactions occur at the surface.[2] Researchers have fabricated varieties of TiO_2 nanoparticle structures comprising zero dimensional (0D) structures, such as spherical nanoparticle,[3] and one-dimensional (1D) structure as nanowire,[4] nanorod,[5] nanobelt,[6] or nanotubes.[7] The titanium dioxide nanotubes are mainly useful in dealing with waste-water due to the large surface to volume ratio. This indeed improves the photocatalytic activity compared with spherical particles under UV-vis irradiations. Numerous efforts have been made towards the fabrication of TiO_2 nanoscale materials with special morphologies *via* employing, for example, sol–gel, micelle, and hydrothermal or solvothermal methods.[8,9] In general, one main drawback of the TiO_2 nanostructures, when used in practical applications, comes from their easy loss during the process of water treatment[9,10] and low adsorption capabilities. This results in low utilization rates and high costs, which limits their widespread use. Some attempts have been made to improve the efficiency of TiO_2 *via* immobilization onto some supports, such as carbon nanotubes,[11,12] glass,[12] ceramic, and activated carbon.[13] However, such immobilization techniques are still not stable enough to improve the reaction efficiency due to decreasing TiO_2 dispersion as well as its leaching from the supports after running periods. Among the previous supports, nanocarbons were chosen as supports to remarkably increase the photoactivity of TiO_2 because it revealed attractive properties,

Benha University, Faculty of Science, Chemistry Department, Benha, Egypt. E-mail: mohmok2000@yahoo.com; Tel: +20 1025384411

† Electronic supplementary information (ESI) available: FTIR spectra of MWCNT and MWCNT–TNT catalysts; effect of reactive intermediates (isopropanol, IPA; *p*-benzoquinone, BQ; triethanolamine, TEOA) on the activity of Au/TNT–MWCNT towards cyclohexane oxidation. Reactions were carried out with 0.05 g of catalyst, 10 mmol cyclohexane, 10 mmol H_2O_2, and 10 mL of acetonitrile, with a photoirradiation time of 12 h (>256 nm). See DOI: 10.1039/c5ra05253j

including exceptional electronic, adsorption, chemical inertness and stability.[14] In recent studies,[15] attention was paid to the fact that TiO_2 is an n-type semiconductor and the major process in photo-catalysis was activated by photon absorption and electron–hole formation. Consequently, an enhancement of the photocatalytic properties of TiO_2 can be accomplished *via* functionalization with CNT and thus hinder electron–hole pair recombination.[13] Additionally, the large number of active adsorption sites at the catalyst surface and the improved suppression of the recombination of the charge carriers contribute to enhancing the photocatalytic activity.[15,16] Many specific methods for the synthesis of TiO_2/CNT composites have been developed, which generally consist of two steps: functionalization of the CNT followed by the composite synthesis.

On the other hand, assembling metal particles either in the wall of titania and/or in carbon nanotubes will indeed enhance their photoelectricity, electromagnetism and catalytic performance.[17] Accordingly, gold catalysts have been successfully used for cyclohexane oxidation based on various supports, including, metal oxides,[18] metal–organic frameworks,[19] mesoporous silica based materials,[20–22] and hydroxyapatite.[23] The great demand for these oxidation products, mainly for cyclohexanol and cyclohexanone, which are key intermediates to adipic acid and caprolactam, and increased environmental concern necessitate the introduction of this catalytic system onto a new gold support as well as using benign oxidants. It has been shown that most gold supported catalysts give conversions in the range of 4% with low selectivity.[24] Some authors support that gold acts as a real catalyst for this reaction[25] while others concluded that it works *via* a pure radical pathway with products typical of auto-oxidation.[26] In general, Au/oxide studies were performed at high temperature (above 373 K) and at oxygen pressures ranging from 0.3 to 3 MPa.[26] On the other hand, titanium based catalysts like titanium silicalite-1 and Ti-MCM-41 when used with H_2O_2 presented low conversion for cyclohexane.[27] V- and Cr-MCM-41 gave higher activities compared to Ti-MCM-41; however, all metallosilicates undergo leaching of the metal and the observed catalytic activity was mainly due to the leached homogeneous metal species.[27,28] The disadvantages of low conversion, leaching of metal, and over-oxidation products in the existed catalytic systems have led us to search for a catalyst that can improve the conversion of cyclohexane under ambient conditions with high selectivity for cyclohexanone/cyclohexanol ratios. Thus, in view of what has been presented and seeking a way of overcoming the mentioned obstacles, titanium dioxide nanotube photocatalysts synthesized by hydrothermal method incorporated with MWCNT and loaded with gold are tested in the photo-oxidation of cyclohexane, for evaluating the effect of surface modification as well as morphology on the catalysts' behaviour. This is attained *via* using the versatile and green oxidant H_2O_2 to avoid using traditional oxidizing agents, such as CrO_4^{2-}, $MnO_4^-$and ClO_4^-, which produce toxic by-products. For comparison purposes, Au/graphene is synthesized and tested for cyclohexane oxidation to determine the effect of easily synthesized graphene of higher conductivity and larger surface area on the catalytic activity.[17]

2. Experimental

2.1. Catalyst preparation

2.1.1. Synthesis of titania nanotubes (TNT). 1.5 g of TiO_2 anatase (Aldrich) was refluxed at 423 K with 100 mL of 10 M NaOH solution for 24 h. This milky suspension was then filtered and washed with aqueous HCl (0.15 M) and distilled water to pH 7, then dried at 373 K for 10 h and finally heated at 623 K for 6 h.

2.1.2. Synthesis of gold supported on titania nanotubes. A specific amount of $HAuCl_4$ dissolved in deionized water was poured onto 1.5 g TNT in a Schlenk tube whilst stirring. To this mixture, 10 mL of 0.1 M Na_2S was added in a dropwise manner, by which the colour changes from yellow to golden brown. 15 mL of PVP (10 g/100 mL) aqueous solution was added to stabilize the final faint rose colour. This mixture was then washed, evaporated at 324 k for 4 h and then heated at 623 K for 6 h.

2.1.3. Acid treatment of MWCNT. 1 g of MWCNT (manufacturer's data: purity > 95%; diameter < 8 nm; length 10–30 μm; S_{BET} > 500 $m^2\ g^{-1}$) was dispersed in 40 mL of 65% HNO_3 followed by agitation at 314 K for 30 min in an ultrasonic bath. This suspension was then transferred into a Teflon lined stainless steel autoclave and stored at 393 K for 24 h, producing a gray precipitate. This precipitate was centrifuged and washed with aqueous HCl (0.1 M) to remove metal impurities, as well as with anhydrous ethanol to remove organic species, followed by drying at 343 K for 12 h. Calculation of the oxidized groups density at the MWCNT surface was done by using the Boehm titration method, resulting in 6.2 mmol g^{-1}.[29]

2.1.4. Synthesis of MWCNT–TNT and Au/MW CNT–TNT nanocomposites. The functionalized MWCNT dispersed in 50 mL of deionized water was poured onto TNT and sonicated for 25 min at 314 K. This suspension was autoclaved at 373 K for 16 h to give a composite comprising 30% MWCNT and 70% TNT. The suspension was then filtered and washed thoroughly with deionized water, then vacuum dried at 343 K for 2 h and finally heat treated in air at 623 K for 6 h to give the MWCNT–TNT composite. An amount of $HAuCl_4$ solution sufficient to prepare 3 wt% Au was added in a dropwise manner onto the suspension of MWCNT–TNT dissolved in 50 mL of water, previously sonicated at 298 K for 1 h, followed by stirring for 1 h at room temperature. This suspension was then reduced *via* hydrazine hydrate to accomplish the complete reduction of Au ions. This suspension was then heated at 333 K for 1 h until complete evaporation, left overnight at 373 K and finally annealed at 623 K for 4 h. Maintaining the heat treatment at 623 K for all synthesized samples even those containing MWCNT was to keep on its existence and to obtain the desired crystallite phase, *e.g.* anatase, while incorporation with TNT. It is expected that 30% CNTs–70% TNT will achieve high activity based on the comparison with CNT–TiO_2 hybrids at the same ratio, which presented high performance for propene oxidation.[8]

2.1.5. Synthesis of graphene-oxide supported gold nanoparticles. Graphene oxide functionalized by COOH and OH groups using the modified Hummers' method was synthesized. More details about the graphene oxide synthesis can be found elsewhere.[30] An adequate amount of $HAuCl_4$ solution to prepare

3 wt% Au was added in a drop wise manner onto a suspension of graphene oxide (GO) dissolved in 50 mL of water followed by stirring for 1 h at room temperature. This suspension was then reduced using hydrazine hydrate to achieve complete reduction of both GO and Au ions. This suspension was then ultrasonicated for 0.5 h and then heated at 333 K for 1 h until complete evaporation. The sample was then heated at 373 K overnight and annealed in air at 623 K for 4 h.

2.2. Catalyst characterization

2.2.1. X-ray diffraction. The X-ray powder diffraction (XRD) patterns of various solids were carried out using a Philips 321/00 instrument. The patterns were run with Ni-filtered Cu Kα radiation ($\lambda = 1.541$ Å) at 36 kV and 16 mA with a scanning speed of 2° in 2θ min^{-1}. The XRD phases present in the samples were identified with the help of ASTM powder data files. The percentages of anatase and rutile were determined by using the intensities of the strongest peaks for anatase and rutile following the equations:[8] $W_R = A_R/0.8844A_A + A_R \times 100$ where $W_R\% + W_A\% = 100$.

2.2.2. N_2 adsorption. The surface properties, namely BET surface area, total pore volume (Vp) and mean pore radius (r), were determined from N_2 adsorption isotherms measured at 77 K using conventional volumetric apparatus. The samples were out-gassed at 473 K for 3 h under a reduced pressure of 10^{-5} Torr before starting the measurement. The total pore volume was taken from the desorption branch of the isotherm at $p/p_0 =$ 0.98, assuming complete pore saturation. The BJH method was accurately used to produce the pore sizes of synthesized materials.

2.2.3. UV-vis diffuse reflectance spectroscopy and Fourier transform infrared (FT-IR) spectroscopy. UV-vis diffuse reflectance spectra of the absorbance of various samples in the 700–300 nm range were obtained using a Jasco V-570 (serial number, C 29635) spectrophotometer attached to a diffuse reflectance accessory. The infrared spectra of the samples were recorded in the range of 400–3000 cm^{-1}. The method includes mixing a few mg of a fine powder of the sample with KBr powder in an agate mortar. The mixture was then pressed by hydraulic press. The transmission was automatically registered against wavenumber (cm^{-1}) using a PerkinElmer instrument (Spectrum GX), made in USA.

2.2.4. Transmission electron microscopy (TEM). TEM micrographs were measured using a Philips Tecani Feil2 at an accelerating voltage of 200 KV. The powder samples were put on carbon foil with a microgrid. TEM images were observed with minimum electron irradiation to prevent damage to the sample structure. SEM (JSM-5200 JEOL, Japan) was used to observe the surface state and structure of the photocatalyst composites. The average particle diameter (d) was calculated using the following formula: $d = \sum n_i d_i / \sum n_i$, where n_i is the number of particle diameter d_i in a certain range, and $\sum n_i$ is more than 100 nanoparticles on TEM images of the sample.

2.2.5. Cyclohexane oxidation. All cyclohexane oxidations were carried out at room temperature according to the following procedures: 0.05 g of catalyst and 10 mmol cyclohexane were put into a 50 mL photochemical reactor; containing 10 mL of acetonitrile, fitted with a cooling jacket. The choice of acetonitrile, rather than acetone, was based on its stability towards light irradiations. Addition of 10 mmol H_2O_2 (30%), which was monitored using iodometric titration, was poured into the system continuously and sealed with a rubber septum cap. Samples were then collected every 1 h after switching on the lamp for a total photo-oxidation period of 12 hours. These experiments were performed in a closed chamber to avoid interference with ambient light. The reactor was placed at the centre of the chamber, equipped with a vent for cooling purposes. The UV mercury lamp was horizontally installed inside the UV chamber, which emits a spectrum called UV-C (296–390 nm). The 125 W power lamp fitted with a long Teflon tube with an average light intensity of 60 mW cm^{-2} was inserted into the reaction solution. More information on the photoreactor can be found elsewhere.[31] The samples collected from every experiment using different catalysts were analyzed by GC-MS. GC-MS analyses were performed using a PerkinElmer Clarus 600C instrument. GC was conducted in temperature-programming mode, using a SGE BPX5 column (25 m × 0.25 mm × 0.25 μm). Reaction products were identified by comparison of their retention times with known reference compounds, and by comparing their mass spectra to fragmentation patterns obtained from the NIST spectral library stored in the computer software of the mass spectrometer. Results show that although cyclohexyl hydroperoxide is an important intermediate component formed during the oxidation of cyclohexane, its selectivity is always kept at a very low level in our experiments, far lower than that of cyclohexanone or cyclohexanol, and the main by-products of the reaction were *n*-butric, *n*-valeric, succinic, glutaric and adipic acid. To study subsequent reuse of the catalysts, the most recently used catalyst was separated from the reaction mixture, washed in alcohol, dried at ambient temperature, and then put into the next catalytic cyclohexane oxidation run. For detecting the active species created in the photocatalytic reaction, hydroxyl radicals ($^{\bullet}OH$), superoxide radical ($^{\bullet}O_2^-$) and holes (h^+) were explored by adding 1.0 mM isopropanol (IPA, a quencher of $^{\bullet}OH$), *p*-benzoquinone (BQ, a quencher of $^{\bullet}O_2^-$), and triethanolamine (TEOA, a quencher of h^+). The interaction of tris(hydroxymethyl) aminomethane (Tris) with hydroxyl radicals ($^{\bullet}OH$) was also performed to provide a simple and convenient assay for detecting $^{\bullet}OH$ generation.[31]

3. Results and discussion

3.1. XRD investigation

The XRD patterns (Fig. 1) show gold loaded titania nanotubes (Au/TNT-inset) as well as gold-free nanotubes following annealing at 623 K. The diffraction lines of the annealed TNT exhibit diffraction lines at 2θ equal 9.5°, 24.01° and 48.4°, representing the (002), (011) and (020) planes, respectively, indexed to $Na_2Ti_2O_5 \cdot H_2O$ of an orthorhombic lattice (Joint Committee of Powder Diffraction Standards (JCPDS) card no. 47-124) structure. The continual washing by 0.1 M HCl prohibits the massive replacement of Na^+ by H^+. Accordingly, an appreciable amount of the brookite phase is depicted *via* existence of the

peak at $2\theta = 30.8°$, assigned to the (211) plane, which represents 17% of total phases constituting titania. In addition, this XRD pattern also indicates significant peaks at $2\theta = 25.3$, 38.0, 48.0, 53.8, 55.1 and 62.7° corresponding to (101), (004), (200), (105), (211) and (204) planes, respectively, assigned to the anatase phase that constitutes 75% of total phases forming titania. A residual existence of the rutile phase (8%) is observed at $2\theta = 27.4°$, which is ascribed to the (110) plane. Notably, no significant changes were shown in the structure following gold incorporation *via* the adopted Na_2S-PVP method (seen as inset) reflecting its good dispersion. However, the broad peak at 9.5°, correlated with the interlayer distance d_{200} in the nanotubes wall, is almost vanished in the 3%Au/TNT sample proposing slight distortion in the crystalline order within the layers due to the ion-exchange process. The mean crystallite size of TNT diffraction peak at $2\theta = 25.3°$ shows higher crystallite growth than that of TNT containing gold, suggesting a strong interaction between gold and TNT.

In order to prepare high activity photocatalysts, multiwalled carbon nanotubes (MWCNT) were added to TNT for modifying the latter photocatalyst. The peaks ascribed to the MWCNT were hardly detected, confirming their dispersion in the nanocrystallite structure of TNT. However, the residual peak at $2\theta = 26.5°$, well indexed to the 002 reflection of graphitic carbons, coincided with that of the MWCNT at the same diffraction angle *i.e.* TNT partially cover the surface of the MWCNT. Interestingly, the enhancement of anatase crystallinity was noticed *via* increasing their peak intensities. Small peaks at $2\theta = 38.4$ and 44.4° were detected for Au^0 corresponding to the (111) and (200) phases in the Au/TNT–MWCNT sample. This latter sample also showed a marked decrease in the intensities of all diffraction lines assigned to the anatase/TNT phase in favour of the brookite one, *via* exposing the peak at 30.8°. The peak intensity decrement in Au/TNT–MWCNT further depicts that TNT–MWCNT was homogenously covered by the Au nanoparticles. In this context, the crystallite sizes of anatase and rutile, determined *via* Scherrer equation, were 12 nm and 16 nm, respectively, lower than that of brookite (18 nm). This figure also shows the XRD pattern of Au/RGO. It proves that GO is reduced to graphene during the treatment with hydrazine hydrate[32] *via* illustrating a broad peak at $2\theta = 25.8°$ corresponding to an interlayer distance of 3.53 Å. The XRD peaks belonging to Au nanoparticles were detected in Au/RGO at $2\theta = 38.5$, 44.4 and 64.5°, corresponding to the (111), (200) and (311) sites, respectively. These characteristic peaks distinguish the fcc structure of gold nanoparticles (Joint Committee on Power Diffraction Standard (JCPDS), File no. 04-0784) of a polycrystalline nature. A comparison between Au/RGO and Au/TNT–MWCNT indicates that Au was highly crystalline on the surface of the former while it was well dispersed on that of the latter due to the decreased intensity of Au crystallites on Au/TNT–MWCNT.

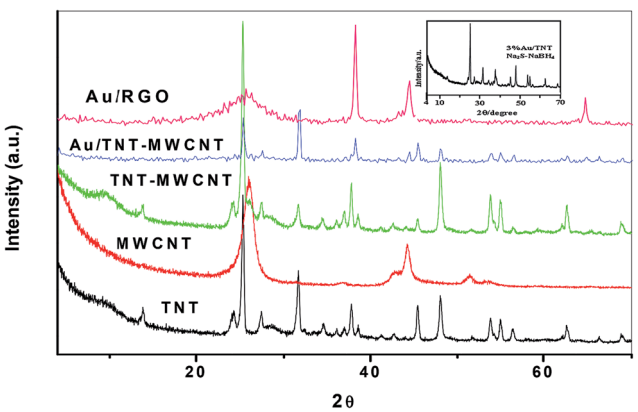

Fig. 1 XRD patterns of TNT, MWCNT, TNT–MWCNT, Au/TNT–MWCNT and Au/GO; the inset is for 3%Au/TNT synthesized using Na_2S-PVP.

3.2. TEM investigation

The TEM image of the 3%Au/TNT sample annealed at 623 K shows a tubular structure with an average diameter of 50 nm and a length equal to 200 nm (Fig. 2a). It seems that the tubular structure is partly damaged as it appears at the peripheral part of the image *via* the presence of spherical nanoparticles. The dark field TEM image seen as an inset elaborates the dispersion of the Au free TNT sample by showing a fibrous product with length equal to several hundreds of nanometres with inner and outer diameters of around 6 and 10 nm, respectively. On the other hand, the inset in Fig. 2a referred to Au/TNT indicates the dispersion of Au nanoparticles of an average diameter of 6 nm inside TNT. The incorporation of MWCNT with 3%Au/TNT affects the tubular structure seen in 3%Au/TNT and changes it into a spindle-like shape (Fig. 2b) with an average diameter of 15 nm and length of 60 nm. As it appears, MWCNT affected the TNT shape by causing a decrease in both the diameter and length related to the 3%Au/TNT sample, proposing an exhibited interaction between MWCNT and TNT. In addition, the agglomeration was decreased upon MWCNT incorporation, proposing that the latter could also act as a spacer for TNT. The in-set image of Au nanoparticles of hexagonal shape and 15 nm diameter shows that Au atoms are mainly not incorporated inside TNT but most probably localized on its surface. In the lower part of the image, CNT is exhibited as free-standing transparent nanotubes, as depicted by HRTEM, indicating that some of them are not well incorporated with TNT. The TEM image of the 3%Au/RGO sample (Fig. 2c) illustrates that the morphology of RGO consists of thin stacked flakes made up of well-defined layers. A homogeneous dispersion of Au nanoparticles of circular shape with an average diameter of 25 nm is depicted in the reduced GO matrix, seen in the inset. The Au nanoparticles are not simply mixed up or blended with RGO; rather, they are dispersed on the RGO sheets.

The FTIR spectra of the oxidized MWCNT and MWCNT/TNT composites are measured to comprehend their interconnection (Fig. S1, ESI†). Bands at 1575, 1653 and 1713 cm^{-1} attributed to C=C, carbonyl and carboxyl, respectively, are exhibited for MWCNT together with an ester group localized as a strong band at 1175 cm^{-1}. The FTIR spectrum of MWCNT–TNT shows

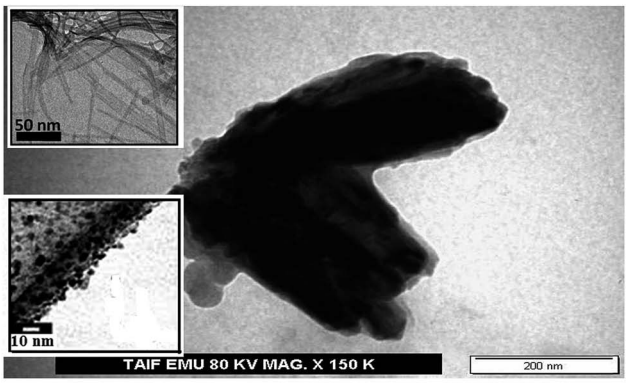

(a)

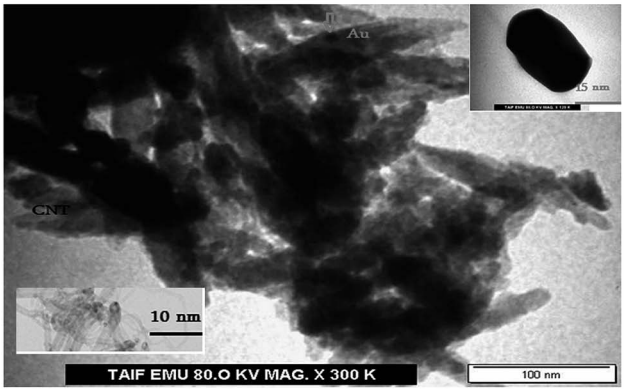

(b)

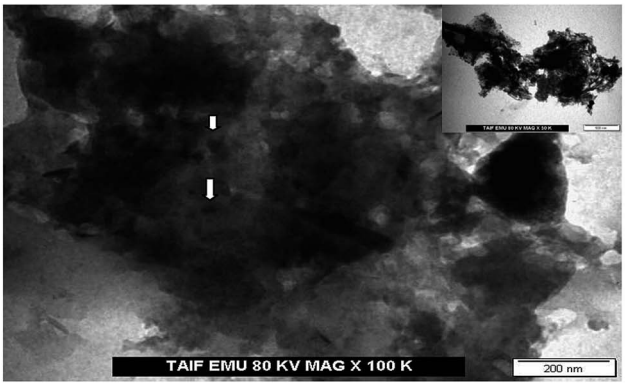

(c)

Fig. 2 TEM images of (a) 3%Au/TNT annealed at 623 K; the upper inset is for pure TNT and the lower inset is for HRTEM of Au/TNT; (b) 3%Au/TNT–MWCNT annealed at 623 K; the inset is for the HRTEM of Au nanoparticles (traced by the red arrow) and HRTEM of MWCNT is in the lower part of the image; and (c) 3%Au/RGO annealed at 673 K where the white arrows represent Au particles; the inset is a TEM image of RGO.

a peak at 700 cm^{-1} due to the Ti–O–Ti vibration beside those exhibited for carbonyl and unsaturated carbon depicted before. The band intensity in the region of the asymmetric carboxylate stretching mode at 1400 cm^{-1} is much higher than that in MWCNT. This assumes that the carboxylate oxygen of CNT interacts with the titanium ion provoking the Ti–O–C bond formation.[33] This result ascertained the hypothesis about the possible interaction between TNT and MWCNT moieties.

3.3. N_2 adsorption

Fig. 3a and b present the N_2 adsorption–desorption isotherms of Au/RGO and Au/TNT–MWCNT, as representative samples, heated at 623 K. They showed type II isotherm with H3 hysteresis loops according to IUPAC classification.[34] These results are confirmed *via* obtaining appreciable values of C in the 20–25 range, and thus omitting any possibility of a type III isotherm, together with the existence of an inflection point at low P/P_o values. The initial part of the isotherm is attributed to monolayer-multilayer adsorption. The Type H3 hysteresis loop observed is characteristic of aggregates of plate-like or slit-shaped pores.[34] The surface properties of synthesized samples determined by N_2 adsorption–desorption measurements are presented in Table 1. The specific surface area, pore volume and pore radius of Au/RGO were determined to be 78.5 $m^2\ g^{-1}$, 0.3 $cm^3\ g^{-1}$ and 15.3 nm, respectively. The hysteresis loop of the latter sample closes at low relative pressures P/P_o equal 0.35. This signifies the presence of large pores as ascertained *via* increasing the pore radius to 15.3 nm. For TNT, the isotherm (not shown) is also of type II with a N_2 hysteresis-loop, characterizing mesoporosity, and discloses a specific surface area equal 72.9 $m^2\ g^{-1}$. The presence of Au in TNT led to a significant decrease in S_{BET} of 17.4% relative to TNT. This proposes that gold blocks some parts of the TNT pores suggesting the good dispersion of gold. Incorporation of MWCNTs into TNT led to a marked increase in surface areas as twice that of the later (Table 1). Accordingly, the pore volume of TNT–MWCNT showed a marked increase comprised of 0.180 $cm^3\ g^{-1}$ compared to 0.135 $cm^3\ g^{-1}$ for TNT, proposing the partial enforcement of MWCNTs inside the TNT pore structure. The noticed decrease in the pore volume of Au/TNT–MWCNT to 0.162 $cm^3\ g^{-1}$ might indicate the good incorporation of Au in the TNT (MWCNT) pores. Accordingly, the average pore diameter showed a decrease in the following order: TNT (19.5 nm) > TNT–MWCNT (17.9 nm) > Au/TNT–MWCNT (17.5 nm). Taking into consideration that the average inner diameter of TNTs determined from TEM measurements was in the range of 30–60 nm, hence the method of nitrogen adsorption underestimates the average diameter of the nanotubes. Accordingly, N_2 adsorption method accounts for the pores inside the tubes rather than the pores between the tubes. These external pores are usually bigger than the internal pores and the size of these pores depends on the way the nanotubes agglomerate into bundles. The adsorption–desorption isotherm of Au/TNT–MWCNT performed by N_2 adsorption at −197 °C confirms that the N_2 adsorption isotherm belongs to type II, in the IUPAC classification. The non-limiting adsorption at high P/P_o is characteristic of Type H3 *i.e.* no limiting adsorption at high P/P_o.

3.4. Light absorption

The light absorption properties of Au containing samples including Au/TNT, Au/TNT–MWCNT and Au/RGO were analyzed by UV-vis diffuse reflectance spectroscopy (Fig. 4) in comparison with Au free ones including TNT and TNT–MWCNT samples. The TNT absorption threshold is localized between

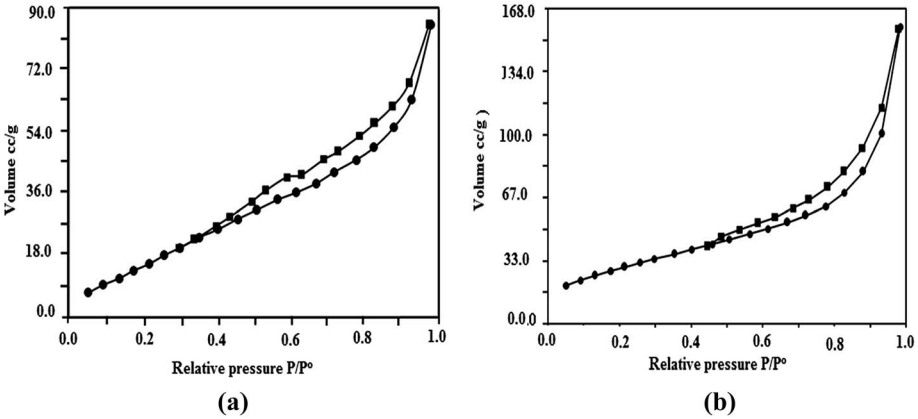

Fig. 3 Adsorption–desorption isotherms of (a) the Au/RGO sample and (b) the Au/TNT–MWCNT sample.

260 and 340 nm with a maximum at 290 nm. On the other hand, the Au/RGO sample coincides with that of the TNT sample in the UV margin. Conversely, the 30%MWCNT–TNT composite absorbs much more light both in UV and visible regions compared with the TNT and Au/RGO samples. This suggests that the introduction of CNT to TNT results in an increment of surface electric charge of the latter.[17] Loading Au on TNT–MWCNT did not change the absorptivity in the UV region of TNT–MWCNT but enhances that of visible light *via* the noticed linear increase towards the visible light to 900 nm. This suggests that the morphologies of Au such as particle size, shape and crystallinity are different from those in the Au/RGO sample, as confirmed from XRD and TEM investigations. In agreement, Au/RGO, Au/TNT–MWCNT and Au/TNT displayed a marked absorption enhancement in both the visible-light and ultraviolet regions, and extended the margin of UV from 260 to 400 nm. The surface plasmon band of the AuNPs is positioned at 520 nm for all gold loaded samples, albeit changing the samples colour from white for TNT to violet in Au/TNT, dark blue in Au/TNT–MWCNT and black in Au/RGO. No change in the wavelength was perceived for all Au containing samples despite changing the support materials.[35,36] The decrease in intensity of plasmon bands in Au/TNT–MWCNT and Au/RGO samples compared with Au/TNT is probably correlated to increasing the irregularity of nanoparticles in the former samples, as depicted from TEM observations.

Table 1 Surface texturing properties of the synthesized catalysts

Sample name	[a]BET Surface area $m^2\ g^{-1}$	[b]Pore volume $Vp\ cm^3\ g^{-1}$	[c]Average pore diameter r nm
TNT	72.9	0.135	19.5
TNT-MWCNT	141	0.180	17.9
Au/TNT	60.2	0.126	18.6
Au/TNT–MWCNT	118.2	0.162	17.5
Au/RGO	78.4	0.30	15.3

[a] S_{BET}; BET surface area. [b] V_p; pore volume. [c] r; BJH adsorption average pore diameter.

3.5. Catalytic performance

The photocatalytic performance of Au based catalysts is evaluated in the selective oxidation of cyclohexane with hydrogen peroxide and the reaction results are summarized in Table 2. It can be noticed that under the same reaction conditions, no conversion is observed in the absence of the catalyst; however, the catalysis is well proceeded with Au as well as with TNT (Fig. 5). This can be obtained based on admitting that gold-based catalysts are active in initiating the cyclohexane oxidation reaction.[26] On the other hand, TiO_2 also showed some activity towards the same reaction, most probably due to the hydroxyl groups exposed on the TiO_2 surfaces, which have been acknowledged to play a major part in this reaction.[37] Catalysts Au/TNT–MWCNT and Au/RGO exhibited the highest activity and selectivity with conversion of 7.5 and 6%, respectively after 12 h reaction.

The Au/TNT–MWCNT Catalyst exhibited a conversion almost double that of Au/TNT. This proposes that MWCNT takes part in this reaction, *i.e.* the morphological and structure order of carbon nanotubes are primer factors affecting the adsorption of organic moieties. It is interesting to note that the selectivity of cyclohexanone and cyclohexanol over Au/TNT–MWCNT was as high as 3.75 (K/A ratio) exceeding those on Au/RGO (2.14), Au/TNT (1.83) and TNT–MWCNT (1.43) catalysts. On the contrary, TNT exhibited the lowest K/A ratio (0.63) due to the absence of Au nanoparticles. Fig. 5 indicates that the conversion increases with time together with cyclohexanone selectivity (Table 2). Interestingly, enhancing the conversion of TNT compared with other mentioned TiO_2 catalysts[38] could be due to the mesoporous character of the TNT surface that maximized the adsorption of the non-polar cyclohexane molecules as well as to the photocatalytically active anatase sites.[20] On the other hand, the open tubular structure of TNT offered a much higher contact area with the facile diffusion of H_2O_2, which is able to form a complex with TiO_2 nanotubes of appreciable Lewis acidity.[39] This response towards H_2O_2 is even increased when Au nanoparticles are embedded in the pores of TiO_2 nanotube, *via* constructing a metal–semiconductor heterojunction.[40] Under illumination, the electric potential difference generated on the

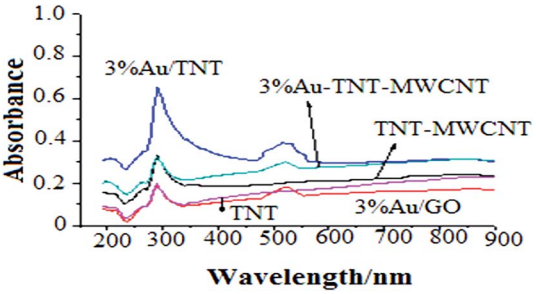

Fig. 4 UV-vis absorption spectra of TNT, TNT–MWCNT, 3%Au/TNT–MWCNT, 3%Au/TNT and 3%Au/RGO samples.

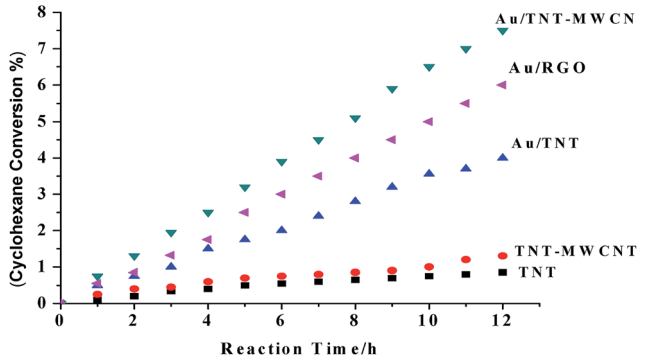

Fig. 5 Cyclohexane conversion *vs.* reaction time on TNT, TNT–MWCNT, Au/TNT, Au/RGO and Au/TNT–MWCNT catalysts. All reactions were done with 0.05 g of catalyst, 10 mmol cyclohexane, 10 mmol H_2O_2, and 10 mL of acetonitrile, with a photoirradiation time of 12 h (>296 nm).

interface of Au/TNT heterojunction assisted the separation of the photogenerated hole–electron pair *i.e.* quickening the transferring rate of the holes and resulting in enhanced photo-oxidation activity.[39–41]

Data shown in Table 2 confirmed the enhancement of cyclohexane oxidation rate on Au/TNT–MWCNT (0.0035 mmol g^{-1} min^{-1}) to higher cyclohexanone production together with lowering the non-selective bi-products formed. On correlating the catalytic performance with the catalyst structure properties, one can deduce that Au nanoparticles (Au^0) are the active sites for the cyclohexane oxidation and the particle size played an important role in the reaction. Catalyst Au/TNT–MWCNT with average Au crystallites of 15 nm, having a hexagonal structure, showed higher activity than Au/RGO with exposed Au crystallites of diameter of 25 nm. Decreasing the Au crystallites size induces an increase in Au active sites, as also confirmed from narrowing the surface plasmon resonance band of Au in Au/TNT–MWCNT comparatively. This indeed will favour the adsorption and activation of the oxygen molecule of H_2O_2 during the oxidation reaction.[41] The observed superior catalytic properties of the catalyst Au/TNT–MWCNT is believed to not only be related to the Au particle size, but also to the surface properties of the support. As cyclohexane is a non-polar organic compound, preferred adsorption into the hydrophobic MWCNT surfaces can be expected. To comprehend the role of MWCNT on the adsorption process, a gravimetric method was employed to determine the equilibrium adsorption capacities of cyclohexane on MWCNT surfaces at room temperature, which indicated a value of 120 mg g^{-1} (12%). Concurrently, it has been shown that the amount of cyclohexane adsorbed before irradiation was the best on Au/TNT–MWCNT that comprised of 15%. This result was in agreement with XRD results, which indicated that the anatase phase that constitutes the highest phase percentages has the lowest crystallites size. In addition, increasing the photocatalytic activity of anatase compared to rutile is well known and related to its better adsorption capacity towards organic compounds. It has been acknowledged before that the rate of $^{\bullet}OH$ formation in aqueous suspension of TiO_2 systems was increased in rutile-containing anatase[42] and this could be the reason for ceasing $^{\bullet}OH$ on Au/TNT–MWCNT that contains 75% anatase. On the other hand, to check whether H_2O_2 molecules are adsorbed and/or activated by Au nanoparticles,[43] the decomposition of H_2O_2 was studied in the dark over Au/TNT–MWCNT as well as under photo-irradiation. To elucidate the hydroxyl radical formation, experiments with scavenger tris(hydroxymethyl)aminomethane (Tris) were performed.[44] It has been shown that $^{\bullet}OH$ radicals were detected in the dark, however this ceased afterwards possibly due to H_2O_2 decomposing into H_2O and oxygen. However, under ultraviolet-irradiation of Au/TNT–MWCNT suspensions, it never stops, at least during the reaction period. These results support the

Table 2 Catalytic properties in selective oxidation of cyclohexane[af]

Catalyst	Cyclohexane conversion (%)	[b]Product selectivity (%)			[c]*K*/*A* ratio	[d]By-products %	[e]Activity (mmol g_{cat}^{-1} min^{-1})
		Cyclohexanol	Cyclohexanone	H_2O_2			
TNT	2.1	51	32	38.2	0.63	17	0.00097
TNT–MWCNT	3.2	35	50	40.3	1.43	15	0.0015
Au/TNT	4	30	55	34	1.83	15	0.0019
Au/TNT–MWCNT	7.5	20	75	45	3.75	5	0.0035
Au/RGO	6	28	60	37	2.14	12	0.0028

[a] All reactions were done with 0.05 g of catalyst, 10 mmol cyclohexane, 10 mmol H_2O_2, 10 mL of acetonitrile, photoirradiation time, 12 h (>256 nm). [b] Selectivity (%) of product = [(concentration of product) × (total concentration of all products) − 1] × 100. Conversion and selectivity calculated based on carbon recovery. [c] K/A: the mole ratio value of cyclohexanone to cyclohexanol. [d] By-products are mainly ring-opened acids, such as *n*-butric, *n*-valeric, succinic, glutaric and adipic acid. [e] The average rate for 12 h of reaction time. [f] H_2O_2 conversion % corresponds to the amount consumed in the reaction.

hypothesis that the hydroxyl radical is the primary oxidant in TiO_2 photocatalysis. It was also shown that TiO_2 activity is enhanced following Au incorporation. This is probably due to the reduction of H_2O_2 on Au/TNT exceeding that on TNT *i.e.* the increase of $^{\bullet}OH$ is attributable to the photocatalytic reduction of H_2O_2, and partly due to Schottky barrier formation at the metal–semiconductor interface.

It has been acknowledged that gold-based catalysts do not show high *K*/*A* (cyclohexanone/cyclohexanol) selectivities (>80%) at high conversions (>7%).[45,46] Our findings in cyclohexane oxidation by Au-based catalysts were inconsistent with the above-mentioned results. This is based on the roles played by TNT in activating and initiating electrons and holes assisted by photo irradiation as well as MWCNT, which evoked the absorbability. CNTs are excellent electric conductors and can so either provide or accept electrons, which are transferred through the Au–TNT interface.[33] For instance, electrons can be photo-induced and easily transferred to the Au–TNT interface, where they are injected into the TNT conduction band. These electrons can trigger the formation of very reactive radicals, such as hydroxyl radicals, which are then responsible for the oxidation reaction, as will be clarified later. More illustration on the contribution of both Au/TiO_2(TNT) and MWCNT towards cyclohexane oxidation can be deduced as follows. An electron–hole pair can be produced between the valence and conduction band of TNT.[47] The photogenerated electrons can be trapped by MWCNT, holding up the recombination process. The trapped electrons could be further transferred to H_2O_2,[48] which is adsorbed on the TNT surface, to generate superoxide radical as well as hydroperoxy ($HO_2^{\bullet}$) and hydroxyl ($^{\bullet}OH$) radicals. It is assumed that the interface between Au and TNT may form an electrical barrier, resulting in the transfer of electrons into Au.[48,49] In addition, increasing the $S_{BET;}$ and pore volume (0.162 $cm^3\ g^{-1}$), of Au/TNT–MWCNT to 118 $m^2\ g^{-1}$ compared to those of TNT and Au/TNT resulted in the best cyclohexane conversion. Concurrently, although Au/RGO exhibited an increase in the pore volume value (into 0.30 $cm^3\ g^{-1}$), it presents a lower activity than that of the latter due to the decrease in S_{BET} value into 78 $m^2\ g^{-1}$ as well as to the absence of TNT structure responsible for light absorption. However, the effectiveness of the RGO based catalyst was unexpected. This enhancement basically depended on the work function change and charge transfer that occur upon cyclohexane adsorption onto π–π graphene networks. Considering the potential of the conduction band (−4.4 eV) and valence band (−7.6 eV) of TNT, graphene (−4.42 eV) and Au nanoparticles (−4.75 eV),[50] a direct electron transfer from adsorbed cyclohexane to graphene semiconductor is not only thermodynamically favourable, but also much more feasible and faster than TNT. This is due to the charge transfer distance from cyclohexane to TNT is longer than with graphene. Convincingly, according to the charge transfer and separation between Au and graphene, an expected electron transfer from Au to graphene is perceived.[51] This results in a separation of electron and phonon transport within this hybrid structure. In this essence, adsorbed cyclohexane on graphene surfaces is promoted photocatalytically.

As illustrated in Scheme 1, H_2O_2 molecules are adsorbed and activated by Au/TNT nanoparticles while cyclohexane molecules preferred the hydrophobic part of the MWCNT surface (Step I). Reaction between the adsorbed cyclohexane and dissociated H_2O_2 produced intermediate cyclohexyl hydroperoxide, which decomposed to form cyclohexanol and cyclohexanone[39] adsorbed on the catalyst (Step II). These oxidation products are further oxidized to byproducts, such as *n*-butric, *n*-valeric, succinic, glutaric and adipic acid, if they do not desorb from the surface promptly. Cyclohexane is preferentially adsorbed over cyclohexanol and cyclohexanone by the Au/TNT–MWCNT catalyst because of the surface hydrophobicity of the catalyst (Step III), thus reducing the probability of deep oxidation. Checking the time-dependent change in the formation of these products was carefully monitored and described that the selectivity for cyclohexanone formation was higher all the time while UV light was on. The selectivity for cyclohexanone/cyclohexanol was completely stopped when light was off proposing that this reaction proceeds due to a photocatalytic effect rather than an over oxidation one. No conversion was seen over any catalyst in the absence of H_2O_2. Indeed, it has been shown that the OH radical produced by photodecomposition of H_2O_2 is the crucial oxidant for cyclohexane oxidation. However, an OH radical can also be produced by the reduction of O_2. It is therefore important to check whether the OH radical was the crucial oxidant or not. The inhibition effect of 2-propanol, which is known as an effective scavenger for hydroxyl radicals was measured. As can be shown (see Fig. S2, ESI†), the rate of cyclohexane oxidation became slower at relatively low concentration of 2-propanol,

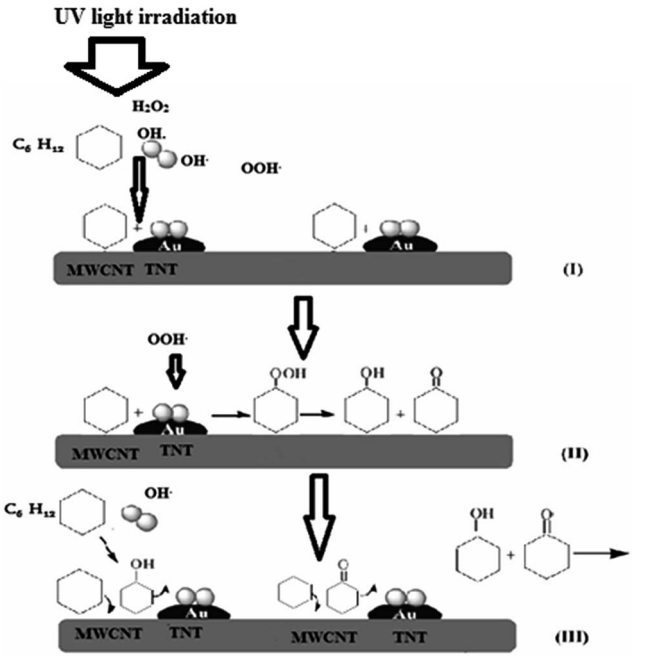

Scheme 1 Proposed mechanism of oxidation of cyclohexane on catalyst Au/TNT–MWCNT. (I) Adsorption and activation of cyclohexane molecules; (II) oxidation of adsorbed cyclohexane to cyclohexanol and cyclohexanone; (III) competing adsorption and desorption of cyclohexane with cyclohexanol and cyclohexanone.

while at a high concentration of 2-propanol, great inhibition was observed indicating, that the hydroxyl radicals are the major active species during the photo-catalytic oxidation reaction. Further trapping experiments for detecting other active species were again conducted during the oxidation of cyclohexane in the presence of Au/TNT–MWCNT under ultraviolet-visible light irradiation. As observed (see ESI†), the oxidation efficiency of cyclohexane was affected by the addition of 1 mM BQ (a quencher of $^{\bullet}O_2^-$) but apparently did not decrease with the addition of 1 mM TEOA (a quencher of h^+). Therefore, these results show that $^{\bullet}OH$ and $^{\bullet}O_2^-$ are the two main active species playing key roles in the oxidation of cyclohexane rather than h^+.

Although gold-based catalysts clearly play a role in directing the oxidation mechanism, it is obvious that the reaction proceeds through a radical-chain mechanism. This was in full agreement with the results published by Xu *et al.*[22] showing that the oxidation reaction over supported Au catalysts would only proceed when *t*-butyl hydroperoxide was initially added as a radical initiator. A radical-chain mechanism directly explains the slow initiation of the oxidation reaction by gold-based catalysts at the very beginning. In order to affirm that the reaction proceeded *via* a radical chain mechanism, hydroquinone (HQ) was used to accomplish whether or not it was a radical involved reaction. At 270 min reaction time when the conversion of 2.5% was reached for catalyst Au/TNT–MWCNT, a specific amount of HQ (0.4 g dissolved in a 1 : 1 CyH : acetonitrile mixture) was added. It was then shown that the amount of products in the liquid phase remained constant between 285 and 300 min (0.5% conversion) followed by ceasing the cyclohexane conversion completely. The strong yellow colour of the liquid-phase sample after HQ addition indicated the formation of benzoquinone, confirming that the reaction proceeds *via* a free radical mechanism.

3.5.1. Effect of amount of H_2O_2. When the amount of H_2O_2 was increased to 15 mmol (keeping all other factors constant) the conversion of cyclohexane increases. The increase in the oxidant amount helps in generating more radicals and thereby increasing the conversion of Au/TNT–MWCNT to 9.0% with the effective use of H_2O_2 reaching 68%. Indeed, this value exceeded several types of Au loaded carbon materials (activated carbon, polymer based carbon xerogels, multi-walled carbon nanotubes, nanodiamonds, micro-diamonds, graphite and silicon carbide). They indicate conversion equal 3.6% (ref. 50) as well as surpassing Au/TiO_2 (ref. 28) and Au/Al_2O_3 (ref. 24) those indicate conversion comprised of 5 and 4%, respectively. The selectivity of cyclohexanone increases to 85% while that for cyclohexanol decreases. This might be due to oxidation of cyclohexanol to cyclohexanone in the presence of excess amounts of H_2O_2. The decomposition of H_2O_2 generates $^{\bullet}O_2^-$ and $HO^{\bullet}$ over gold metal as well as on TNT,[52] as explained previously. Such radicals abstract hydrogen from cyclohexane forming cyclohexyl radicals. This unstable peroxide dissociates *via* two separate processes to give cyclohexanol and cyclohexanone. However, increasing the amount of H_2O_2 to 20 mmol causes reaction termination and thus the efficiency of H_2O_2 decreases into 43%.

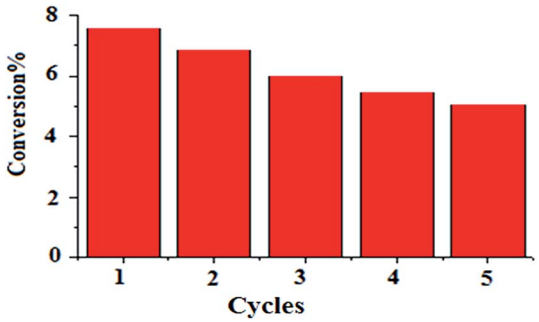

Fig. 6 Repeated cycles up to 5 times illustrating the conversion yield of cyclohexane after 12 h over the Au/TNT–MWCNT photocatalyst. All reactions were done with 0.05 g of catalyst, 10 mmol cyclohexane, 10 mmol H_2O_2, and 10 mL of acetonitrile, with a photoirradiation time of 12 h (>296 nm).

3.5.2. Catalyst recyclability. The regenerated catalyst showed only a slight decrease in the conversion of cyclohexane following the fifth run, as shown in Fig. 6. It showed a decrease from 7.5 to 5.7% conversion proposing the preserve of active sites even after this long period that extends into 60 h. The recovered supported catalyst attained *via* filtration was only washed with acetonitrile and dried at 333 K for 2 h before further use in the next run. The presence of different types of sites on the catalyst surface can be considered. These could be related to the titanium nanotube that acts as Lewis acid sites, due to their low coordination, as well as light harvesting together with gold nanoparticles are considered as strong adsorption sites, suitable for both cyclohexane and H_2O_2 moieties. The second type could be the hydrophobic MWCNT and its synergistic role with TNT those committed to cyclohexane adsorption and charge transfer between them. Moreover, the filtrate solution test (an additional 24 h of reaction after removing the Au/TNT–MWCNT photocatalyst from the reaction medium) showed no catalytic activity, indicating that leaching did not play an important role in the present system. The above experiment shows that Au/TNT–MWCNT functions as a high performance photocatalyst under the present reaction conditions.

4. Conclusions

It has been shown that gold nanoparticles (15 nm, hexagonal shape) dispersed on TNT–MWCNT composites prepared by hydrothermal deposition method exhibited higher photocatalytic (125 W, λ = 296–400 nm) activity towards cyclohexane oxidation at ambient conditions in the liquid phase (conversion = 7.5%) and k/A oil selectivity exceeding Au/RGO and Au/TNT catalysts. The activity can reach conversion of 9% by increasing the H_2O_2 concentration to 15 mmol. The oxidation of cyclohexane into the main products, cyclohexanone and cyclohexanol, on the former catalyst was repeated at least five times without significant loss in either conversion or selectivity values. This was attributed to the uniform dispersion of Au nanoparticles on the mesoporous TNT support, enhancement of cyclohexane adsorption onto the MWCNT hydrophobic surface and to the surface texturing properties of the composite TNT–MWCNT. A

competing adsorption and desorption mechanism was used to explain the high K/A oil selectivity on the catalyst prepared using the mentioned method. One should state that improving the capability of this new kind of catalyst demands more in-depth experimental work to enhance the activity. More important correlations about the mechanism and the activity of the catalysts in view of their performances under UV illuminations with the experimental results were developed and discussed.

References

1 S. Iijima, *Nature*, 1991, **354**, 56–58.
2 N. G. Chopra, R. J. Luyken, K. Cherrey, V. H. Crespi, M. L. Cohen, S. G. Louie and A. Zettl, *Science*, 1995, **269**, 966–968.
3 Y. Feldman, E. Wasserman, D. J. Srolovitz and R. Tenne, High-Rate, *Science*, 1995, **267**, 222–225.
4 P. M. Ajayan, O. Stephan, Ph. Redlich and C. Colliex, *Nature*, 1995, **375**, 564–567.
5 H. Nakamura and Y. Matsui, *J. Am. Chem. Soc.*, 1995, **117**(9), 2651–2652.
6 P. Hoyer, *Langmuir*, 1996, **12**, 1411–1413.
7 T. Kasuga, M. Hiramatsu, A. Hoson, T. Sekino and K. Niihara, *Adv. Mater.*, 1999, **11**, 1307–1311.
8 N. Bouazza, M. Ouzzine, M. A. Lillo-Rodenas, D. Eder and A. Linares-Solano, *Appl. Catal., B*, 2009, **92**, 377–383.
9 P. Hoyer, *Langmuir*, 1996, **12**, 1411–1413.
10 W. C. Oh, *J. Korean Ceram. Soc.*, 2009, **46**, 234–241.
11 G. H Du, Q. Chen, R. C. Che, Z. Y. Yuan and L. M. Peng, *Appl. Phys. Lett.*, 2001, **79**, 3702–3704.
12 S. Hasegawa, Y. Sasaki and S. Matsuhara, *Sens. Actuators, B*, 1993, **13–14**, 509–510.
13 R. Kumar, S. K. Sithambaram and S. L. Suib, *J. Catal.*, 2009, **262**, 304–313.
14 Q. H. Zhang, L. A. Gao, J. Sun and S. Zheng, *Chem. Lett.*, 2002, **31**, 226–227.
15 G. H. Du, Q. Chen, R. C. Che, Z. Y. Yuan and L. M. Peng, *Appl. Phys. Lett.*, 2001, **79**, 3702–3704.
16 K. Woan, G. Pyrgiotakis and W. Sigmund, *Adv. Mater.*, 2009, **21**, 2233–2239.
17 K. A. Wepasnick, B. A. Smith, K. E. Schrote, H. K. Wilson, S. R. Diegelman and D. H. Fairbrother, *Carbon*, 2001, **49**, 24–36.
18 H. F. Gorgulho, J. P. Mesquita, F. Gonc-alves, M. F. R. Pereira and J. L. Figueiredo, *Carbon*, 2008, **46**, 1544–1555.
19 R. Pasricha, S. Gupta and A. K. Srivastava, *Small*, 2009, **5**, 2253–2259.
20 M. Conte, X. Liu, D. M. Murphy, K. Whiston and G. J. Hutchings, *Phys. Chem. Chem. Phys.*, 2012, **14**, 16279–16285.
21 Z. G. Sun, G. Li, L. P. Liu and H. O. Liu, *Catal. Commun.*, 2012, **27**, 200–205.
22 L.-X. Xu, C.-H. He, M.-Q. Zhu, K.-J. Wu and Y.-L. Lai, *Catal. Commun.*, 2008, **9**, 816–820.
23 X. Jiang, H. Deng and X. Wang, *Colloids Surf., A*, 2010, **358**, 122–127.
24 L. X. Xu, C. H. He, M. Q. Zhu and S. Fang, *Catal. Lett.*, 2007, **114**, 202–210.
25 Y. Liu, H. Tsunoyama, T. Akita, S. Xie and T. Tsukuda, *ACS Catal.*, 2011, **1**, 2–6.
26 C. Della Pina, E. Falletta and M. Rossi, *Chem. Soc. Rev.*, 2012, **41**, 350–369.
27 A. Alshammari, A. Koeckritz, V. N. Kalevaru, A. Bagabas and A. Martin, *ChemCatChem*, 2012, **4**, 1330–1336.
28 B. P. C. Hereijgers and B. M. Weckhuysen, *J. Catal.*, 2010, **270**, 16–25.
29 E. V. Spinace, H. O. Pastore and U. Schuchardt, *J. Catal.*, 1995, **157**, 631–639.
30 W. A. Carvalho, P. B. Varaldo, M. Wallau and U. Schuchardt, *Zeolites*, 1997, **18**, 408–412.
31 G. Strukul, *Catalytic Oxidations with Hydrogen Peroxide as Oxidant*, Kluwer Academic Publishers, Dordrecht, 1992.
32 H. P. Boehm, *Carbon*, 1994, **32**, 759–769.
33 M. M. Mohamed and M. S. El-Sharif, *Appl. Catal., B*, 2013, **142–143**, 432–441.
34 M. M. Mohamed, S. A. Ahmed and K. S. Khairou, *Appl. Catal., B*, 2014, **150–151**, 63–73.
35 G. M. Lu, D. Ji, G. Qian, Y. X. Qi, X. L. Wang and J. S. Suo, *Appl. Catal., A*, 2005, **280**, 175–180.
36 M. M. Ibrahim, S. A. Ahmed, K. S. Khairou and M. M. Mohamed, *Appl. Catal., A*, 2014, **475**, 90–97; I. Bannat, K. Wessels, T. Oekermann, J. Rathousky, D. Bahnemann and M. Wark, *Chem. Mater.*, 2009, **21**, 1645–1653.
37 I. Jung, D. A. Dikin, R. D. Piner and R. S. Ruoff, *Nano Lett.*, 2008, **8**, 4283–4287.
38 A. Maldotti, A. Molinari and R. Amadelli, *Chem. Rev.*, 2002, **102**, 3811–3836.
39 K. Bhattacharyya, A. Danon, B. K. Vijayan, K. A. Gray, P. C. Stair and E. Weitz, *J. Phys. Chem. C*, 2013, **117**, 12661–12678.
40 P. Du, J. A. Moulijn and G. Mul, *J. Catal.*, 2006, **238**, 342–352.
41 K. Shankar, J. I. Basham, N. K. Allam, O. K. Varghese, G. K. Mor, X. Feng, M. Paulose, J. A. Seabold, K.-S. Choi and C. A. Grimes, *J. Phys. Chem. C*, 2009, **113**, 6327–6359.
42 P. Wu, P. Baia, K. P. Loh and X. S. Zhao, *Catal. Today*, 2010, **158**, 220–227.
43 J. T. Carneiro, J. A. Moulijn and G. Mul, *J. Catal.*, 2010, **273**, 199–210.
44 C. B. Almquist and P. Biswas, *Appl. Catal., A*, 2001, **214**, 259–271.
45 M. M. Mohamed, M. T. Salama and M. Ichikawa, *J. Colloid Interface Sci.*, 2000, **224**, 366–371.
46 H. Zhang and P. X. Feng, *Carbon*, 2010, **4**(8), 359–364.
47 A. W. Musumeci, E. R. Waclawik and R. L. Frost, *Spectrochim. Acta, Part A*, 2008, **71**, 140–142.
48 W. Yongmei, J. Zhang, L. Xiao and F. Chen, *Appl. Catal., B*, 2009, **88**, 525–532.
49 W. Su, S. S. Wei, S. Q. Hu and J. X. Tang, *J. Hazard. Mater.*, 2009, **172**, 716–720.
50 S. A. C. Carabineiro, L. M. D. R. S. Martins, M. Avalos-Borja, J. G. Buijnsters, A. J. L. Pombeiro and J. L. Figueiredo, *Appl. Catal., A*, 2013, **467**, 279–290.
51 J. Xiang and L. T. Drzal, *ACS Appl. Mater. Interfaces*, 2011, **3**(4), 1325–1332.
52 T. Harifi and M. Montazer, *Appl. Catal., A*, 2014, **473**, 104–115.

